Research Square

Preprints are preliminary reports that have not undergone peer review.
They should not be considered conclusive, used to inform clinical practice,
or referenced by the media as validated information.

Interaction Mechanism of Tunnel Excavation and Overlying Building Loads in Shallow-Buried Coastal Urban Tunnels

Hanming Zhang
China University of Geosciences (Beijing)
Zhuangzhuang Guo
China University of Geosciences (Beijing)
Fanmeng Kong
kongfanmeng10@cugb.edu.cn
China University of Geosciences (Beijing)
yiguo Xue
China University of Geosciences (Beijing)

Article

Keywords: Shallow-buried extra-large-span tunnel, coastal urban areas, Overlying building loading, Fluid-solid coupling, Tunnel-building interaction

Posted Date: September 29th, 2026

DOI: https://doi.org/10.21203/rs.3.rs-10719480/v1

License: This work is licensed under a Creative Commons Attribution 4.0 International License.
Read Full License

Additional Declarations: No competing interests reported.

Version of Record: A version of this preprint was published at Scientific Reports on November 19th, 2026. See the published version at https://doi.org/10.1038/s41598-026-81270-x.

Interaction Mechanism of Tunnel Excavation and Overlying Building Loads in Shallow-Buried Coastal Urban Tunnels

Hanming Zhang[1, 3], Zhuangzhuang Guo[1, 2, 3], Fanmeng Kong[1, *], Yiguo Xue [1, *]

[1]*School of Engineering and Technology, China University of Geosciences (Beijing), Beijing 100083, China*

[2]*Institute of Geotechnical and Underground Engineering, Shandong University, Jinan 250061, China*

[3]*These authors contributed equally*

*Corresponding authors:

Fanmeng Kong, E-mail: kongfanmeng10@cugb.edu.cn

Yiguo Xue, E-mail: xueyiguo@cugb.edu.cn

Abstract: The onshore sections of subsea tunnels in coastal urban areas are highly susceptible to excavation-induced deformation because of shallow cover, large span, complex strata, groundwater, and surcharge from overlying buildings. However, the response mechanism governing the interaction between tunnel excavation and overlying building loading remains insufficiently understood. This study investigates the onshore section of the Second Qingdao Jiaozhou Bay Subsea Tunnel through geomechanical model tests, coupled hydro-mechanical numerical simulations, and in-situ monitoring. The results show that excavation sequence and groundwater seepage govern tunnel deformation and ground settlement. Excavation of the upper bench beneath the building is identified as the most critical stage, producing the greatest stress release, pore-pressure dissipation, and surface settlement. Groundwater seepage significantly amplifies deformation, increasing crown settlement by up to 27.3% due to excavation-induced drainage in water-rich strata. Building loading further increases settlement above the tunnel and narrows the settlement trough. When the tunnel is offset from the building, the settlement profile becomes asymmetric, and the building experiences tilting and additional structural strain during undercrossing. These findings highlight the importance of incorporating groundwater effects and three-dimensional tunnel-building interaction into the design and construction of shallow-buried, large-span tunnels in coastal urban areas.

Keywords: Shallow-buried extra-large-span tunnel; coastal urban areas; Overlying building loading; Fluid-solid coupling; Tunnel-building interaction.

1. Introduction

Subsea tunnels are important transportation infrastructures for crossing straits and bays in coastal cities. During construction, significant deformation is frequently observed in the surrounding rock, particularly in the onshore sections of subsea tunnels. This phenomenon may result from the complexity of coastal strata, including artificial fill, rock heterogeneity, and differential weathering [1, 2]. In addition, compared with offshore sections, the onshore sections of subsea tunnels are typically characterized by shallow burial depth, large span, and construction beneath densely built urban areas. The coupling of these factors may exert a significant influence on the deformation characteristics of the surrounding rock [3, 4].

Large deformation of the surrounding rock in subsea tunnels may lead to collapse hazards, posing a severe threat to workers' safety and causing huge financial losses [5, 6]. Due to the shallow-buried nature of such tunnels, tunnel collapse may ultimately induce surface subsidence. Both rock/soil deformation and ground subsidence make surface buildings highly vulnerable to damage, which may further provoke social unrest [7, 8]. For example, on 7 February 2018, during the construction of Foshan Metro Line 2, collapse of the overlying urban roadway was triggered by failure of the shield machine tail seal, resulting in 11 fatalities, 8 injuries, and a direct economic loss of 53.238 million CNY. On 1 December 2019, a crown water-inrush and collapse occurred in a mined tunnel of Guangzhou Metro Line 11, leading to 3 fatalities and an economic loss of approximately 20.047 million CNY. On 12 December 2019, a surface collapse occurred at the Lvcuo intersection associated with Xiamen Metro Line 2, forming a large sinkhole of about 500 m² in area and 7 m in depth, into which two private cars fell.

Accordingly, many useful methods have been developed to explore the tunnel

deformation mechanism caused by excavation or adjacent building loading. One notable example is the geomechanical model test, which uses a scaled model to simulate engineering geological problems based on the principle of similitude.

The critical importance of similar materials in reproducing the deformation behaviour of tunnel rock and soil masses has been recognized for several decades [9, 10, 11]. Li et al. developed a new type of similar material for fluid-solid coupling model tests in underground engineering, and this material can simulate rock-like materials with different strengths and permeabilities [12]. Moreover, the testing system is indispensable for conducting model tests, and many studies have focused on stress/seepage loading devices, tunnel excavation simulation equipment, and monitoring systems [13, 14, 15].

In particular, various studies have addressed the interaction between tunnel excavation and surface construction activities. For example, Ritter et al., using centrifuge model tests, demonstrated that soil-structure interaction during tunnel excavation is highly reproducible and further identified building layout, aspect ratio (height-to-width ratio), and façade openings as the primary factors governing building responses to tunnelling [16]. Foundation construction is also a common issue to consider when evaluating tunnel deformation characteristics. Xu et al. compared raft foundations with separate footing foundations and attempted to reveal the mechanism of tunnel-framed building interaction [17]. This line of research was later extended by Liu et al., who studied the effects of foundation pit excavation on the deformation patterns of existing tunnels using model tests. It was found that foundation pit excavation tends to induce tunnel displacement toward the excavation, and that the shallower the tunnel burial depth, the more pronounced the deformation [18].

Moreover, numerical analysis has been recognized as another useful method for studying the influence of building loading on tunnel deformation [19]. This is exemplified by the finite element method, which was used by Ding et al. to characterize the three-dimensional deformation of existing buildings caused by tunnelling. Their study indicated that, under various working conditions, foundation settlement generally experiences three stages: slow increase, rapid increase, and gradual stabilization [20]. Similarly, Namazi et al. used ABAQUS to analyse the three-dimensional behaviour of buildings subjected to tunnel-induced ground movement. They noted that investigations of tunnel-building interaction should not be limited to plane-strain analysis; when the tunnel is skewed relative to the building, additional three-dimensional deformations, such as building torsion, may further exacerbate the structural demand and stress state of the building [21].

Many factors, such as building foundation type, tunnel horizontal distance, and tunnel alignment, influence the deformation of surface buildings [22, 23, 24, 25]. These studies implied that the horizontal distance between the tunnel and the building is the dominant factor controlling the vertical deformation of the building. Moreover, the differential settlement of the building is characterized by more pronounced settlement at the rear side, i.e., the side along the tunnelling direction, and reaches its maximum when the excavation face advances to the midspan of the building.

In recent years, disaster-related problems in water-rich tunnel scenarios, including

subsea tunnels [26], coastal tunnels [27], and cross-river tunnels [28], have attracted increasing attention. Existing studies indicate that excavation disturbance induces stress redistribution, while water-rich conditions lead to pore-pressure dissipation. In weak strata, the bearing capacity is further reduced, causing tunnel construction in such environments to face more complex boundary conditions.

Fluid-solid coupling analysis is an important approach for investigating the excavation response of tunnels in water-rich strata. Zhao et al., based on a hydro-mechanical coupling analysis of excavation in fractured porous rock masses, pointed out that, compared with models considering only mechanical responses, fluid-solid coupling leads to more significant damage propagation, fracture displacement, and pore-pressure disturbance [29]. Using the Gongbei Tunnel of the Hong Kong-Zhuhai-Macao Bridge as a case study, Zhang et al. revealed that, under weak muddy strata and high groundwater-table conditions, ground-surface displacement is highly sensitive to construction method. Their findings further indicate that construction of large-section tunnels in coastal water-rich environments must account for the coupling relationship between groundwater control and stratum response [30].

As a result, building responses induced by tunnel excavation have been extensively investigated, and fluid-solid coupling approaches for water-rich tunnel conditions have also become relatively mature. However, under seepage conditions in coastal environments, the feedback mechanism between stratum deformation and building response during staged excavation remains insufficiently understood.

To address this limitation, the Second Qingdao Jiaozhou Bay Subsea Tunnel was selected as the representative case. A research framework integrating a coupled hydro-mechanical model test system, fluid-solid coupling numerical simulation, and in-situ monitoring was established. On this basis, the critical construction stage responsible for significantly amplified deformation response was identified, the amplifying effect of groundwater conditions on the feedback process was clarified, and the asymmetric deformation response induced by the three-dimensional spatial relationship between the tunnel and the building was revealed. The findings of this study are expected to provide a theoretical basis for understanding the interaction mechanism between tunnel excavation and overlying building loading, thereby supporting the design of tunnel support schemes, effectively reducing the risk of building settlement, and improving construction safety.

2. Methods

2.1. Study site and engineering geology

The onshore section of the Second Qingdao Jiaozhou Bay Subsea Tunnel (the world's longest undersea highway tunnel) is located in Huangdao District, Qingdao City (see Fig. 1). This tunnel section has a total length of 346 m and is characterized by a shallow burial depth (17.26-20.35 m) and an extra-large span (20.44-29.93 m). At the tunnel site, the surface soil consists of highly heterogeneous artificial fill with a thickness of 0.2-9.50 m, composed of sandy soil, clay, and rock debris. The underlying strata are marine and alluvial deposits. The bedrock is granite with varying degrees of weathering, ranging from highly weathered to moderately weathered and slightly weathered in the vertical direction. The groundwater mainly consists of phreatic water

and bedrock fissure water, and the groundwater table depth ranges from 1.30 to 3.60 m.

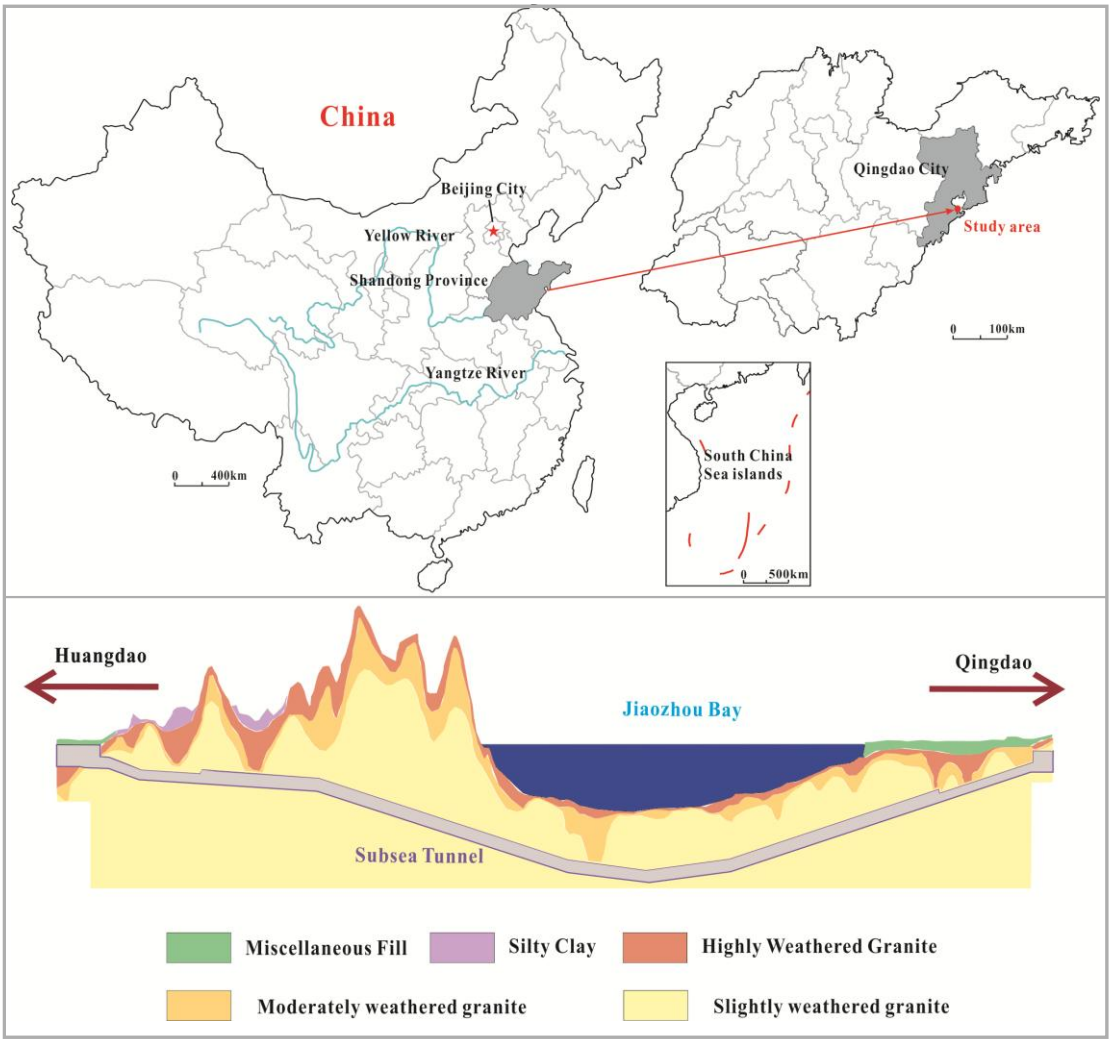

Figure 1. Geological setting of the Second Qingdao Jiaozhou Bay Subsea Tunnel. The figure shows the geographic location of the onshore section and the strata intersected by the tunnel.

Moreover, along this onshore section, the tunnel passes beneath two surface buildings. One is a single-story brick-concrete structure with a strip foundation, and the distance between its foundation and the tunnel crown is 13.62 m. The other is an eight-story reinforced concrete frame structure with an isolated foundation, whose foundation is 11.62 m above the tunnel crown. Ground and building settlements were monitored during the tunnelling process to provide guidance for the safety protection of the overlying buildings.

2.1.1. Physical and mechanical properties of the tunnel surrounding rock

The geological conditions of the study section are complex, and the specific physical and mechanical properties are summarized in Table 1. The overlying fill and fluvial-alluvial silty clay generally exhibit low strength and small modulus, and are highly sensitive to disturbance. The interbedded sandy layers increase permeability and dilatancy, which may easily induce seepage and localized sand boiling.

Table 1

Physical and mechanical parameters of strata

Stratum name	Unit weight (kN/m³)	Poisson's ratio	Elastic modulus (MPa)	Internal friction angle (°)	Cohesion (kPa)	Permeability coefficient (m/d)
Miscellaneous fill	19.5	0.34	8	20	26	25
Moderately to slightly weathered granite	25.6	0.15	38,500	40	100	0.8

Due to the long-term influence of in-situ geological stress, the surrounding rock has developed distinct weathering zones from top to bottom. The slightly weathered rock mass remains relatively intact and has higher strength and stiffness. The moderately weathered rock is characterized by more developed joints and reduced integrity. The highly weathered rock has transformed into a sandy and friable material. The structurally fractured rock, composed of sandy and blocky breccias formed by tectonic activity, is extremely fragmented and therefore constitutes a critical zone for stability and seepage control in large-span sections.

2.2. Geomechanical model test

2.2.1. Similarity scales

The similarity scale, denoted by the letter C , has been widely recognized as the basis for developing similar materials for model tests. It is defined as the scaling relationship between the physical prototype (p) and the geomechanical model (m). In this study, L denotes length, r denotes unit weight,δ denotes displacement, σdenotes stress,ε denotes strain, σ^t denotes tensile strength, σ^c denotes compressive strength,c denotes cohesion, φ denotes internal friction angle, μ denotes Poisson's ratio, E denotes elastic modulus, t denotes time, K denotes permeability coefficient. According to similarity theory, the similarity scales of physical quantities can be derived using the following relationships:

For all dimensionless physical quantities, the similarity scale is equal to 1, including strain, internal friction angle, and Poisson's ratio, i.e.,

$$C_\varepsilon=C_\varphi=C_\mu=1 \tag{1}$$

For physical quantities with the same dimensions, the similarity scales are identical, including stress, strength, and elastic modulus, i.e.,

$$C_\sigma=C_{\sigma^c}=C_{\sigma^t}=C_E \tag{2}$$

Based on the equilibrium equation, the similarity relationship among the stress similarity scale C_σ, the unit weight similarity scale C_r, and the geometric similarity scale C_r can be expressed as

$$C_rC_L/C_\sigma=1 \tag{3}$$

Based on the geometric equation, the similarity relationship among the geometric similarity scale C_L, the strain similarity scale C_ε, and the displacement similarity scale C_δ can be expressed as

$$C_LC_\varepsilon/C_\delta=1 \tag{4}$$

Based on the physical equation, the similarity relationship among the stress

similarity scale C_σ, the strain similarity scale C_ε, and the elastic modulus similarity scale C_E can be expressed as

$$C_\sigma / C_\varepsilon C_E = 1 \tag{5}$$

According to fluid-solid coupling similarity theory, the similarity relationship among the geometric similarity scale C_L, the unit weight similarity scale C_r, and the permeability coefficient similarity scale C_K can be derived as

$$C_K = \sqrt{C_L} / C_r \tag{6}$$

Based on Newton's second law and dimensional analysis, the similarity relationship between the time similarity scale C_t and the geometric similarity scale C_L can be derived as

$$C_t = \sqrt{C_L} \tag{7}$$

In this study, the geometric similarity scale was set to 75. The detailed similarity scales of the physical quantities are listed in Table 2.

Table 2

Similarity condition and scale of model test.

Physical Quantity	Similarity Condition	Expression
Geometric dimension	$C_L = L_p / L_m$	$C_L = 75$
Bulk density	$C_r = r_p / r_m$	$C_r = 1$
Displacement	$C_\delta = C_L C_\varepsilon$	$C_\delta = 75$
Stress	$C_\sigma = C_L C_r$	$C_\sigma = 75$
Strain	$C_\varepsilon = \varepsilon_p / \varepsilon_m$	$C_\varepsilon = 1$
Internal friction angle	$C_\varphi = \varphi_p / \varphi_m$	$C_\varphi = 1$
Cohesion ratio	$C_\mu = \mu_p / \mu_m$	$C_\mu = 1$
Elastic modulus	$C_E = C_\sigma / C_\varepsilon$	$C_E = 75$
Time	$C_t = \sqrt{C_L}$	$C_t = 8.7$
Permeability coefficient	$C_K = \sqrt{C_L} / C_r$	$C_K = 8.7$

2.2.2. Similar materials

The similitude requirements for mechanical and hydraulic properties are different, and it is difficult for natural materials to satisfy both simultaneously. Therefore, this study independently developed model materials that satisfy the similitude requirements

of the Second Qingdao Jiaozhou Bay Subsea Tunnel by controlling the similarity of key parameters, including unit weight, UCS, tensile strength, elastic modulus, internal friction angle, cohesion, and permeability.

For the moderately to slightly weathered granite, iron powder, barite powder, and quartz sand were selected as aggregates; white cement was used as the binder; 1000 cSt silicone oil was adopted as the permeability regulator; and water served as the mixing agent. The overlying fill layer was simulated using river sand, barite powder, calcium carbonate, and water.

Fluid-solid coupling in similar materials must satisfy not only hydraulic conductivity similarity, but also the similarity requirements for strength and deformation [26]. The optimal proportions of the components were determined through orthogonal tests. The final mix designs were as follows: the similar material for moderately to slightly weathered granite consisted of 21% iron powder, 42% barite powder, 21% quartz sand, 10% white cement, and 6% silicone oil; the similar material for miscellaneous fill consisted of 28% river sand, 56% barite powder, 8% calcium carbonate, and 8% water. Finally, laboratory tests were conducted to evaluate the physico-mechanical properties of the developed similar materials. Table 3 lists the physical and mechanical parameters of the actual rock mass and the model materials.

Table 3

Physical and mechanical parameters of the actual rock mass and the model materials

Physical and mechanical parameters	Moderately to slightly weathered granite	Similar material for granite	Miscellaneous fill	Similar material for miscellaneous fill
Unit weight (kN/m3)	25.6	25.61	19.5	19.13
Internal friction angle (°)	78.10	1.39	25.3	31.87
Cohesion (kPa)	38500	513.00	27.6	0.375
Permeability coefficient (10^{-6}cm/s)	57.80	4.20	28.9	3.25

2.2.3. Model test system

In this study, a custom-designed experimental model and testing method were developed to simulate the stepwise excavation of a large-span tunnel beneath adjacent buildings, in order to investigate the deformation feedback mechanism of a shallow-buried, large-span tunnel in a coastal urban area. The model test system is illustrated in Fig. 2 and consists of the following components:

(1) Model box. The geometric similarity ratio was 1:75. The frame dimensions were 100 cm × 100 cm × 100 cm (length × width × height). The side panels were made of transparent high-strength acrylic glass with observation windows, and a tunnel portal was pre-reserved in the steel plate at the excavation face to facilitate stepwise excavation and backfilling.

(2) Building structural units. A strip-foundation brick-masonry structure, simulating a laboratory building, was fabricated from gypsum materials, with dimensions of 33 cm × 20 cm × 6 cm. An eight-story frame structure with isolated foundations was constructed using acrylic components, with overall dimensions of 320

mm × 270 mm × 370 mm. The floors and beams were made of acrylic plates and rigidly connected. The physical and mechanical parameters of the building model materials are listed in Table 4.

Table 4

Physical and mechanical parameters of building model materials

Structural Unit	Unit Weight (kN/m3)	Axial Tensile Strength（MPa）	Axial Compressive Strength （MPa）	Poisson's Ratio	Elastic Modulus (GPa)
Initial Shotcrete Support	25	1.27	11.9	0.2	30.0
Rock Bolt	78	-	-	0.2	200.0
Foundation	25	1.57	16.7	0.2	36.6
Slab Beam	25	1.43	14.3	0.2	33
Beam	25	1.10	9.6	0.2	28

(3) Building loading device. The loading device consisted of a bidirectional hydraulic cylinder mounted at the top, together with a loading beam, steel plates, oil pipes, and force sensors. To simulate the surcharge imposed by the overlying building, the target building load for the model was determined in accordance with the Load Code for the Design of Building Structures and similarity theory. For the prototype eight-story frame structure, the floor live load was 2 kN/m² and the dead load was 5 kN/m². By converting the isolated foundations into an equivalent strip foundation, the equivalent floor load of the prototype building was obtained as p_0=8.8kPa. Since the elastic modulus of the prototype reinforced concrete structure is approximately 10 times that measured for the acrylic building model, the distributed load similarity coefficient was taken as C_p=10. Accordingly, the target vertical load of the eight-story frame building model can be expressed as

$$F_1=p_0abn/C_p \tag{8}$$

where F_1 is the target vertical load of the building model (N), a and b are the transverse and longitudinal dimensions of the building model (m), respectively, and n is the number of stories. The calculated target load was 0.609 kN. In the test, a constant-load control mode was adopted. Including the self-weight of the building model, the target load was applied and maintained using the hydraulic loading device while the tunnel was excavated step by step, thereby simulating the sustained action of building loading throughout the construction process.

(4) Groundwater pressurization device. In this model test, fluid-solid coupling was achieved through the physical interaction among groundwater pressure applied by this device, seepage flow through the permeable similar materials, excavation-induced stress release, and the formation of drainage boundaries during excavation. The device consisted of a water tank, a loading unit, and an inlet-outlet pipeline system. It was capable of applying sustained constant-pressure loading, with a maximum pressure of

0.5 MPa.

2.2.4. Model test procedure

Based on the similitude scaling, the applied stress was imposed on the model building from above using a loading beam and a bearing plate. A load-controlled scheme of 0.01 kN/s was adopted, with stepwise loading and a holding time of 1 min at each step, until the target load of 0.609 kN was reached. In addition, hydraulic pressure was applied in stages using a water-pressure loading device, with an increment of 0.01 MPa per stage over 10 min. The next stage was applied after the pressure had stabilized, until 0.1 MPa was reached. The final pressure was maintained for 24 h to establish a stable seepage field.



Figure 2. Geomechanical model test system. **a** Complete test system; **b** model box and loading assembly; **c** data acquisition system; **d** surface building model; and **e** sensors used in the test.

To monitor the multi-physical-field responses of surrounding rock displacement, stress, and seepage, as well as the mechanical responses of the buildings during excavation of a large-span tunnel adjacent to structures in a coastal urban area, various sensors were employed. These included displacement meters, dial gauges, earth pressure cells, piezometers, and surface strain gauges attached to the building model.

To ensure the generality of the test results, three monitoring sections were established in the model test. During the simulated tunnelling beneath the buildings,

monitoring was conducted when the tunnel face reached positions beneath the front wall, directly beneath the building, and beneath the rear wall. The effects of staged excavation sequence and building type on tunnel-ground-building deformation interaction were examined under pressurized groundwater conditions. The monitoring-point layout is shown in Fig. 3b.

Dial gauges for settlement, surface strain gauges, and inclinometers were installed between the stories of the building model. Along the lower surface of the building, settlement dial gauges were arranged at horizontal intervals of 20 cm. Within the influence zone beneath the building, five displacement monitoring points were arranged horizontally in each section. Along the vertical direction through the building centerline and above the tunnel crown, displacement, vertical stress, and pore pressure monitoring points were installed at vertical intervals of 7.5 cm. On both sides of the tunnel periphery, horizontal monitoring lines were arranged for displacement, pore pressure, and stress, with a horizontal spacing of 10 cm between adjacent points on each line.

To minimize mutual interference caused by the dense layout of monitoring elements, the horizontal and longitudinal monitoring lines were alternately staggered during sensor installation. After embedding, the sensor cables were laid horizontally to the inner wall of the model box and then routed outward through outlets on the side wall. The monitoring points were numbered using the format "monitoring type + index", increasing sequentially from left to right and from top to bottom. For example, G1 denotes the surface settlement at key point 1, D2 represents the vertical ground displacement at key point 2, S3 corresponds to the stress at key point 3, and P4 denotes the pore water pressure at key point 4.

Before excavation, the lateral geostress, the equivalent building load, and the groundwater pressure were first applied and maintained until the readings at all monitoring points became stable. The stable readings recorded by the earth pressure cells and piezometers were taken as the initial stress field and initial seepage field, respectively. Stepwise excavation was then carried out.

Excavation was simulated using the CD (central diaphragm) method. The tunnel diameter in the model was 26.6 cm, and the excavation advance was 4 cm per step. A staggered excavation scheme was adopted between the upper and lower benches, with a staggered advance of 6-10 cm. The left pilot tunnel was excavated first, followed by the right pilot tunnel, until all sequential excavation steps had passed the monitored section (see Fig. 3a).

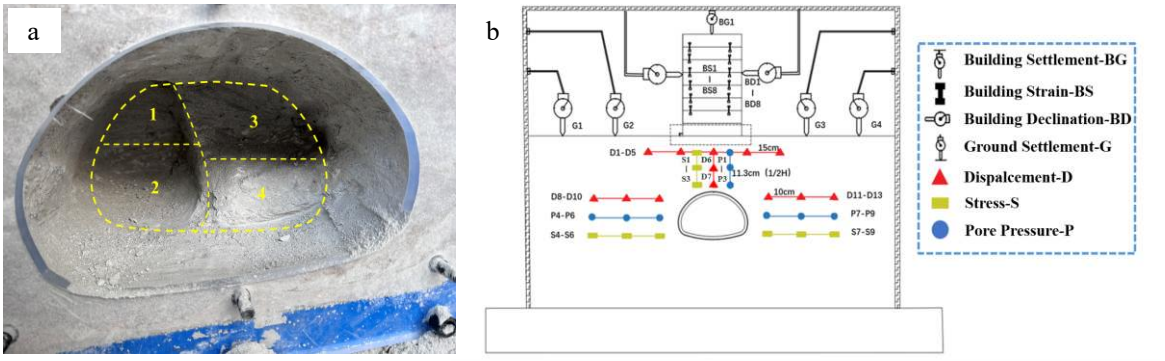

Figure 3. Excavation and monitoring configuration of the geomechanical model test. **a** Simulated excavation sequence using the central diaphragm (CD) method; **b** layout of monitoring points.

In addition, the monitoring zone was arranged at the centre of the model box, with a net distance of approximately 1.38D from each side boundary. The influence of boundary effects on the dominant deformation mechanism was therefore considered acceptable, although it remains one of the limitations of the present model test.

2.3. Numerical simulation

2.3.1. Numerical model setup

In this study, a numerical model of a shallow-buried, extra-large-span tunnel and its overlying buildings in a coastal urban area was established using the finite difference method implemented in GTS NX. In the analysis, the rock-soil mass was assumed to be an isotropic and homogeneous continuous medium. Groundwater seepage was assumed to follow Darcy's law and to satisfy the equivalent continuous seepage condition in all directions. Before excavation, the pore water was assumed to be in a steady state, and the surrounding rock below the groundwater table was taken to be fully saturated. After tunnel excavation, the seepage field was allowed to redistribute and evolve under seepage conditions. The initial stress field of the numerical model considered only self-weight stress, while tectonic stress was not taken into account.

As shown in Fig. 4, and following the Saint-Venant principle, the lateral boundaries were placed at 3-5 times the tunnel diameter from the excavation contour line (D = 20 m). The distance from the tunnel invert to the bottom boundary was set to three times the tunnel height. The model domain measured 120 m in width and 60 m in height. The tunnel crown was located 15 m below the ground surface. The strata consisted of mixed fill soil overlying slightly weathered granite, with the tunnel body entirely embedded in the granite layer.

An eight-story reinforced concrete frame building was adopted as the structural model. The beams and columns of the frame structure measured 300 mm × 300 mm and 500 mm × 500 mm, respectively, and the floor thickness was 120 mm. C25 concrete was used for all structural members. Based on field measurements, the physico-mechanical parameters of the ground and building model materials are listed in Table 4.

In this study, the surrounding rock mass of the tunnel was modelled as an elastic-plastic material using the Mohr-Coulomb constitutive model and its modified form. The initial shotcrete lining was simulated using two-dimensional elastic plate elements, while the rock bolts were represented by one-dimensional elastic rod elements.

For the displacement boundary conditions, normal constraints were applied to the front, back, left, and right boundaries of the numerical model, no constraints were applied at the top boundary, and fixed constraints were imposed at the bottom boundary.

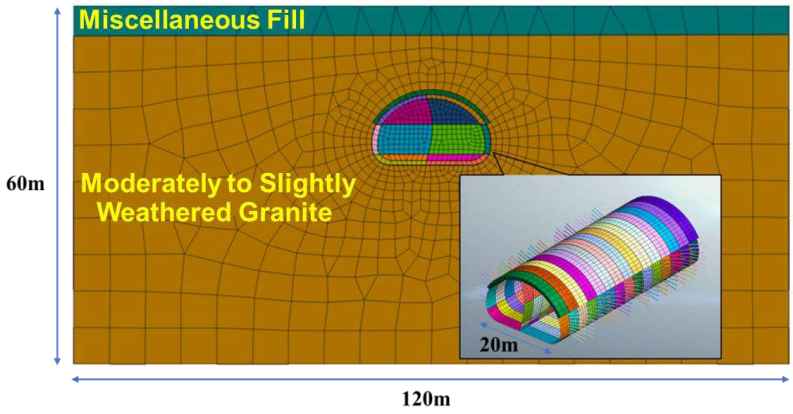

Figure 4. Numerical model of the tunnel-ground-building system. The figure shows the model geometry, stratigraphy, boundary dimensions and overlying frame building used in the coupled analysis.

For the seepage boundary conditions, the most unfavorable conditions were assumed, with the soil-rock mass in a saturated state. The four side boundaries and the bottom boundary of the numerical model were set as impermeable, while the top boundary was set as a free boundary. The water head in the model was defined as pressure head, and boundary water head was applied to the vertical sides of the model.

The construction process of the shallow-buried, large-span tunnel in the coastal urban area was simulated using the CD method. The excavation sequence was divided into four stages: (1) excavation of the upper bench of the left pilot tunnel; (2) excavation of the lower bench of the left pilot tunnel; (3) excavation of the upper bench of the right pilot tunnel; and (4) excavation of the lower bench of the right pilot tunnel. The excavation advance was 3 m per cycle, and initial support with temporary bracing was applied after each sub-step within the same cycle.

To compare and analyse the deformation and mechanical response characteristics of tunnel-building interaction under the influence of groundwater seepage and overlying buildings, the numerical simulation scheme included five working cases:

Case 1: The building is located directly above the tunnel, and the tunnel excavates along the longitudinal axis of the building.

Case 2: The building is offset by 0.5 times the tunnel diameter (10 m) from the tunnel centerline, and the tunnel intersects the building from the side.

Case 3: The building is offset by 1 time the tunnel diameter (20 m) from the tunnel centerline, and the tunnel intersects the building from the side.

Case 4: The angle between the tunnel excavation direction and the building's longitudinal axis is 45°, and the tunnel obliquely intersects the building.

Case 5: The angle between the tunnel excavation direction and the building's longitudinal axis is 90°, and the tunnel passes directly beneath the building.

3. Results

3.1. Geomechanical model test results

3.1.1. Evolution of displacement, stress, and seepage pressure

Figure 5a shows the evolution of vertical displacement at the tunnel crown. Owing to excavation-induced redistribution of the stress and seepage fields, the displacement

field changed markedly and rapidly, most notably at the crown section. During excavation of the lower bench of the left pilot tunnel, the maximum displacements at D3, D6, and D7 were 9.75 mm, 12.75 mm, and 14.25 mm, respectively. By the end of excavation, the maximum displacement reached 33.75 mm at the crown gauge D7. Notably, the dominant deformation at D7 occurred during excavation of the upper bench of the right pilot tunnel as it advanced through the monitored section. When the excavation face was 4 cm ahead of the section, the cumulative displacement was 21 mm, increasing to 31.5 mm as it passed the section, representing an increase of approximately 50% and accounting for 31% of the total cumulative deformation. These results indicate that unloading associated with excavation of the upper bench of the right pilot tunnel exerts a pronounced influence on crown settlement. Similar deformation trends were observed at D3 and D6.

The displacement histories at the springline gauges D8-D13 on the left and right sides. Gauges D8-D10 are located on the left-pilot side and were therefore more strongly affected by Stages I and II. The maximum cumulative displacement at D8 was 7.5 mm, accounting for approximately 90% of its final value, while the maxima at D9 and D10 were 19.5 mm and 22.5 mm, respectively. Gauges D11-D13, located on the right-pilot side, exhibited smaller pre-displacements under the disturbance caused by left-pilot excavation in Stages I and II, with pre-displacements of approximately 5.25 mm (D11), 4.5 mm (D12), and 1.5 mm (D13). Excavation of the upper bench of the right pilot tunnel had the greatest effect on vertical deformation on the right side, yielding cumulative displacements of 16.5 mm (D11), 13.5 mm (D12), and 2.25 mm (D13).

Figure 5b shows the stress evolution at the tunnel crown. As shown in Fig. 5b, excavation of the upper benches of both pilot tunnels produced more pronounced stress disturbance at the crown. Under the combined effects of excavation unloading and groundwater seepage, the stresses at S2 and S3 exhibited an overall decreasing trend with substantial fluctuations, whereas S1 showed smaller fluctuations but remained at a relatively high level. For S3, which exhibited the most significant variation, the major stress release occurred as the upper bench of the right pilot tunnel advanced across the monitored section, with stress decreasing from about 225 kPa at Section I to approximately 22.5 kPa at Section II. The stress evolution at S3 can be divided into three stages: quasi-linear release, rapid release, and quasi-stable behaviour.

Because the signals at the outer springline gauges were weak, except for S6 and S7, only the vertical stresses at S6 and S7 are discussed here. Stress release was mainly concentrated during upper-bench excavation of the left and right pilot tunnels, showing a stepwise decrease with regular fluctuations but without abrupt stress drops. At S6, when Stage I excavation passed directly beneath the building, the stress increased slightly from 252 kPa to 256 kPa, indicating brief stress accumulation. After completion of Stage I, it decreased from 252 kPa to 145 kPa, corresponding to a release ratio of approximately 42%. Compared with the crown, upper-bench excavation induced stronger disturbance at the springline. After Stage III excavation, the stresses at S6 and S7 tended to stabilize.

Figure 5c shows the evolution of seepage pressure in the surrounding rock, which

followed a three-stage pattern of "gradual decrease-sharp decrease-stabilization". Before the excavation reached the monitored section beneath the building, seepage pressure exhibited only slight attenuation and remained essentially stable. Once excavation reached the section and formed a free surface, it decreased from approximately 86 kPa to about 78.5 kPa. During excavation of the lower bench of the left pilot tunnel, seepage pressure remained relatively stable. However, during excavation of the upper bench of the right pilot tunnel, pronounced stepwise dissipation occurred, with seepage pressure dropping sharply from 78.5 kPa to approximately 37.5 kPa, accompanied by intensified crown seepage and accelerated pore-pressure dissipation. After completion of section excavation, seepage pressures at all gauges stabilized at low values, with some gauges approaching complete dissipation and P4 and P9 stabilizing at approximately 7.5 kPa. Overall, pore-pressure dissipation at the crown was greater and faster than that at the springline, and upper-bench excavation contributed more to seepage-pressure dissipation than lower-bench excavation.

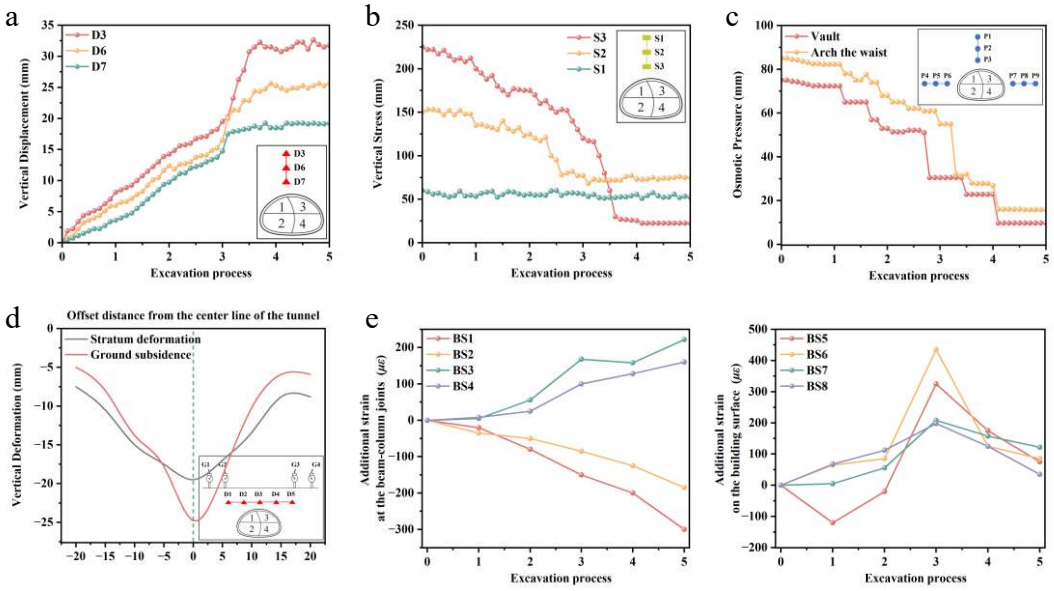

Figure 5. Measured tunnel-ground-building responses during staged excavation. **a** Vertical displacement at tunnel-crown monitoring points; **b** stress at tunnel-crown monitoring points; **c** seepage-pressure evolution in the surrounding rock; **d** ground-surface settlement trough and stratum deformation; and **e** additional strain at ground-floor beam-column joints and on the building surface.

3.1.2. Stratum settlement and deformation of overlying buildings

Figure 5d shows the deformation of the strata above the tunnel and the settlement trough curves of the ground surface beneath the overlying building. Before and after application of the building load, the maximum settlement occurred at monitoring point D3 directly above the tunnel centerline, reaching approximately 19.5 mm. During excavation, the settlements at points D1 and D2 were about 15.0 mm and 17.25 mm, respectively. Owing to the earlier excavation of the left pilot tunnel and the associated stress release, the vertical settlement on the left side was relatively larger than that on the right side. Comparison with the ground-surface measurements at G1-G5 indicates that building loading intensified surface settlement, with the influence mainly confined

within approximately 0.5D on either side of the tunnel centerline. Relative to the stratum deformation, the surface settlement trough remained nearly symmetric, while the curve became narrower and deeper. In particular, excavation of the upper bench of the right pilot tunnel induced a marked increase in surface settlement, and the maximum settlement at G3 on the tunnel axis rose sharply from 16.5 mm to 24.8 mm.

Tunnel excavation exerted a significant influence on the settlement and mechanical response of the overlying building (see Table 5). When the advancing face approached the front edge of the building, the predominant deformation was tilting toward the excavation direction. As the tunnel face passed directly beneath the frame structure, the building exhibited forward tilting, and the magnitude of deformation reached its maximum. Once the tunnel face had completely passed beneath the structure, the tilting deformation decreased slightly and then stabilized.

Table 5

Settlement difference and distortion of each corner of frame structure.

Excavation Procedure	Settlement Difference(mm)				Distortion Deformation(mm-1)
	$s_1 - s_2$	$s_3 - s_4$	$s_1 - s_3$	$s_2 - s_4$	
1	0.1	0.7	0.5	0.2	1.041×10^{-5}
2	1.0	2.5	1.8	0.8	2.894×10^{-5}
3	1.4	4.6	3.6	1.2	6.481×10^{-5}
4	0.8	2.0	1.6	1.0	2.083×10^{-5}

Figure 5e shows the additional strains induced in the frame structure by tunnel excavation, excluding the initial strains generated during the application of the external building load. When tunnelling advanced to Stage I beneath the building, negative compressive strains were recorded at gauges BS1 and BS2 on the front surface of the vertical frame beams. When excavation reached Stage III beneath the building, positive tensile strains developed at gauges BS3 and BS4 on the rear surface of the vertical frame beams (see Fig. 5e). In addition, as excavation passed directly beneath the building, the additional surface strains measured at BS5-BS8 reached their peak values. Owing to the influence of the right-side excavation sequence, the strain responses at BS6 and BS7 exhibited a certain lag. The most pronounced strain change was first observed on the front surface at BS5, whereas the response at BS8 on the rear surface lagged behind that at BS5 (see Fig. 5e).

3.2. Numerical simulation results

3.2.1. Evolution of displacement field in the tunnel surrounding rock and settlement of surface buildings

Representative vertical displacement distributions for Cases 2 and 4 are shown in Fig. 6a,b. In all cases, the deformation patterns of the surrounding rock were generally consistent, with the maximum settlement at the crown reaching approximately 28.9 mm. Laterally, the vertical displacement extended outward from the crown and propagated toward the ground surface at an angle, reaching up to 1.5D from the tunnel centerline. Excavation of the upper bench of the right pilot tunnel had the greatest influence on displacement evolution. The surface settlement troughs were generally wide and flat,

519 although the trough center was slightly offset. The maximum settlement first increased
520 and then decreased under the influence of the overlying building. With increasing
521 intersection angle α, the settlement trough became narrower and the magnitude of
522 deformation decreased significantly.
523 Crown displacement and ground-surface settlement were compared across the five
524 cases. As the building was progressively offset from the tunnel centerline, the
525 magnitude of crown settlement decreased only slightly, and a tendency for reverse
526 radial deformation of the tunnel was observed during the load-offset process. With
527 increasing crossing angle α, the settlement over the entire excavation cycle increased,
528 stress was released more rapidly, and the response entered a stable stage earlier.
529 In terms of surface settlement, Case 1 showed an overall uniform settlement with
530 a maximum value of 20.6 mm. In Case 2, eccentric loading developed, increasing the
531 maximum settlement to 28.7 mm and shifting the settlement curve to the left. In Case
532 3, the building load mainly acted on the soil mass to the right of the tunnel, inducing
533 local ground heave and shifting the settlement curve to the right. The maximum heave
534 was 0.6 mm, while the maximum settlement decreased by 3 mm. As the crossing angle
535 α increased, the overall deformation level decreased markedly, and the settlement at the
536 trough bottom decreased from 28.9 mm to 19.8 mm.
537 Representative building settlement distributions for Cases 4 and 1 are shown in
538 Fig. 6c,d, respectively. As the tunnel offset increased, the settlement pattern shifted
539 from central symmetry to inclination toward the left side, with the greatest effect
540 occurring within the 0-0.5D range. With increasing angle between the tunnel excavation
541 direction and the building's longitudinal axis, the settlement distribution evolved from
542 symmetric to skewed and became concentrated near the structural corners. This was
543 accompanied by larger settlement values and a more localized distribution.

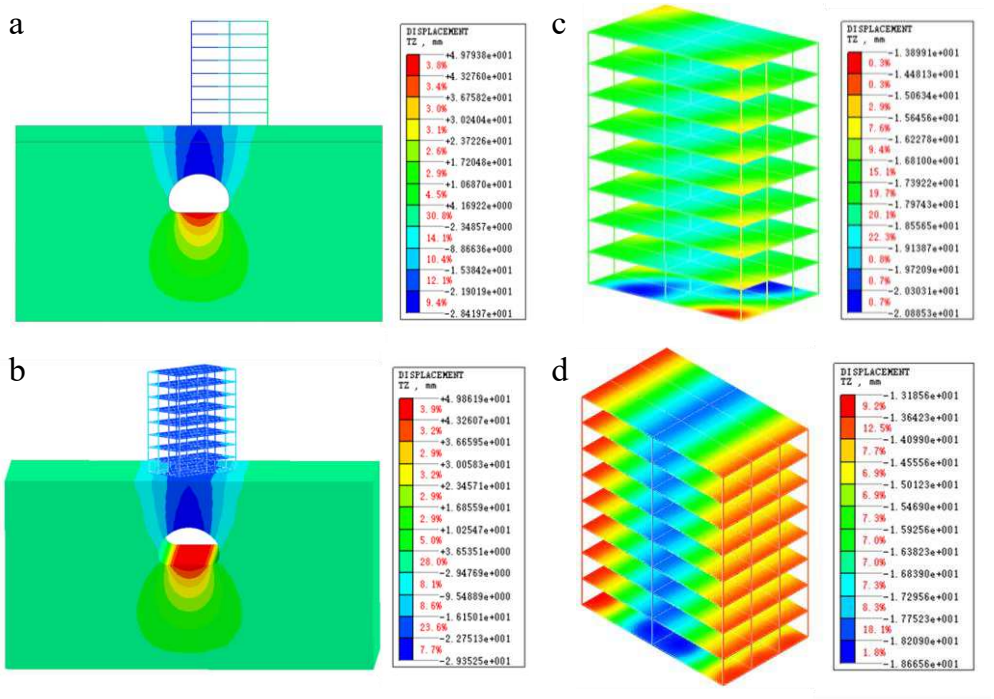

544

545 **Figure 6.** Vertical displacement and structural settlement under selected tunnel-building

configurations. Overall vertical displacement for **a** Case 2 (0.5D tunnel offset) and **b** Case 4 (45° crossing angle); building settlement for c Case 4 and d Case 1 (building directly above the tunnel).

3.2.2. Evolution of stress in the surrounding rock and mechanical response of surface buildings

The first and third principal-stress distributions after fluid-solid coupling are shown in Fig. 7a,b. Tunnel excavation caused significant stress redistribution, while the surrounding rock remained in a compressive state and clear stress concentrations were observed at the crown and arch foot. The vertical stress at the crown monitoring point decreased from 185 kPa to 82 kPa. The stress evolution can be divided into three stages: uniform release, sharp change, and stabilization. After excavation of the right pilot tunnel in Procedure 3, the stress state at the crown stabilized. Groundwater significantly amplified stress variations, increasing both the release range and the extreme values of the first and third principal stresses. The most pronounced changes occurred at the arch foot and crown, where the risk of local instability was greatest.

Additional stresses in the building were primarily induced by differential settlement of the foundation, which dominated structural load redistribution. The bending-moment distribution of the building frame is shown in Fig. 7c. With increasing beam inclination and torsional deformation of slabs, the maximum axial force occurred near the central column on the ground floor and decreased with greater tunnel offset and changes in crossing angle. The maximum shear force was concentrated at the connection between the foundation and the first-floor beam-column joint. The shear forces under working conditions 1-5 before and after excavation were 75.2 kN, 74.8 kN, 72.5 kN, 92.8 kN, and 107.2 kN, respectively. The maximum bending moment occurred at the foundation beam-slab-column joint, where stress concentration was most evident. As the angle between the building's longitudinal axis and the tunnel decreased, the variation in bending moment tended to stabilize.

3.2.3. Evolution of seepage pressure in the surrounding rock

The post-excavation pore water pressure distribution is shown in Fig. 7d. With stepwise tunnel excavation and installation of drainage holes, the seepage field underwent significant changes. Seepage vectors became more concentrated around the tunnel crown and arch foot, with excavation of the upper bench of the right pilot tunnel exerting the greatest influence. During excavation, the pore water pressure at the crown and arch shoulder dropped sharply from 137.2 kPa to 50.9 kPa. Upon completion of excavation, the pore water pressure nearly dissipated and stabilized, ultimately forming a precipitation funnel. These changes in the seepage field exerted a marked influence on the stress distribution and deformation of the surrounding rock.

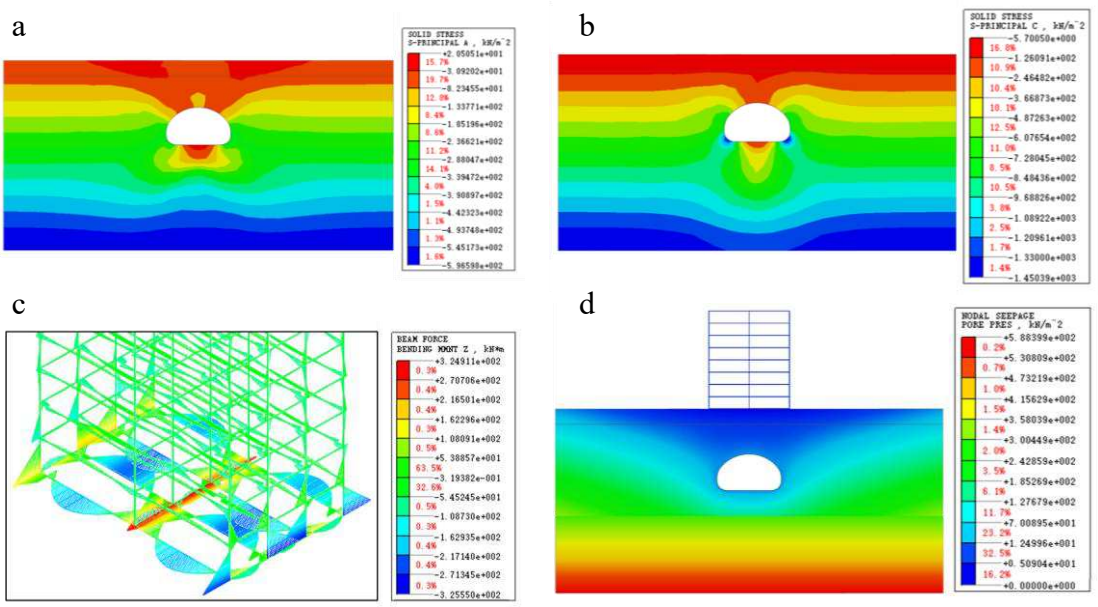

Figure 7. Coupled mechanical and hydraulic responses of the tunnel-building system. **a** First and **b** third principal stress after fluid-solid coupling; **c** bending-moment distribution in the building frame; and **d** pore water pressure after tunnel excavation.

4. Discussion

4.1. Critical deformation stage and its formation mechanism

Both the geomechanical model test and the numerical simulation indicate that the section beneath the overlying building is the most sensitive control zone for tunnel-ground-structure interaction, and that excavation of the upper bench of the right pilot tunnel corresponds to the most unfavorable response. At this stage, crown settlement, surface settlement, stress release, and pore-pressure dissipation are all most pronounced, indicating that the key to deformation development is not a single factor, but rather the concentrated superposition of multi-field responses under staged excavation conditions.

Compared with excavation of the lower bench, excavation of the upper bench more directly weakens the confinement of the surrounding rock near the crown, making this zone more susceptible to rapid unloading. When this process occurs directly beneath the building, the elevated initial stress level induced by the building load is redistributed within a short period of time, thereby synchronously intensifying crown displacement, surface settlement, and additional structural strain. Meanwhile, excavation of the upper bench of the right pilot tunnel takes place after the left pilot tunnel and the preceding excavation stages have already disturbed the ground. As a result, the medium affected at this stage is no longer the initial surrounding rock, but rather a rock mass that has already experienced partial unloading and pore-pressure adjustment, thus exhibiting a clear cumulative disturbance effect.

4.2. Fluid-solid coupling effects in water-rich strata

Groundwater conditions in coastal strata are an important factor that significantly amplifies the excavation response. Figure 8a shows a clear coordinated evolution between pore water pressure and displacement at the crown during construction: when pore pressure dissipates slowly, displacement increases relatively gradually; when pore pressure enters a stage of rapid dissipation, crown settlement accelerates accordingly.

The underlying mechanism is that excavation alters the hydraulic boundary conditions of the surrounding rock, gradually creating drainage paths that are more favorable near the crown and arch shoulders. During the early stages of construction, pore pressure decreases in a stepwise manner, and deformation remains relatively limited. However, when excavation advances into the building-controlled zone and a more fully developed free-drainage surface is formed, local seepage becomes significantly intensified, pore pressure dissipates rapidly, and the effective stress state is consequently altered, thereby inducing additional compression and settlement. The numerical results further show that seepage is mainly concentrated near the crown and arch foot. When groundwater is taken into account, the maximum crown displacement increases by 27.3% compared with the case without seepage, indicating that groundwater not only increases the final magnitude of deformation, but also intensifies the abrupt response during the critical stage. Because pore-pressure dissipation is faster and unloading is stronger at the crown, deformation is more readily transmitted upward to the overlying strata and building foundations. Therefore, in coastal water-rich strata, deformation control should focus on local changes in drainage conditions during upper-bench excavation and their amplifying effect on deformation.

4.3. Regulating role of spatial relationship in stratum and structural responses

Building loading and its spatial relationship with the tunnel can significantly alter the morphology of the settlement trough and the mode of structural response. When the building is located directly above the tunnel, the ground-surface settlement trough remains approximately symmetric overall, but becomes deeper and narrower under the effect of building loading. This is because the building load modifies the transmission path of excavation-induced disturbance in the shallow strata, causing settlement to become more concentrated near the trough bottom.

When the building is offset from the tunnel centerline, the superposition relationship between the load-concentrated zone and the excavation-induced unloading zone changes. As a result, the settlement trough evolves from an approximately symmetric form into an asymmetric distribution, while the building response changes from overall settlement to differential settlement and tilting deformation. Changes in the crossing angle further enhance three-dimensional effects, making additional internal force concentration more likely to occur at building corners, foundations, and beam-column joints on the first floor. In the model test, additional strain was more pronounced at the lower-floor joints, while in the numerical simulation, axial force, shear force, and bending moment were also mainly concentrated at the foundation and critical locations on the first floor. These results indicate that the spatial relationship controls not only the magnitude of settlement, but also the distribution pattern of unfavorable structural responses. Therefore, for offset or oblique undercrossing conditions, the assessment should not be limited to maximum settlement alone, but should also consider differential settlement, tilting, torsion, and local stress concentration.

4.4. Cross-validation with field monitoring, engineering implications, and limitations

Figures 8b and 8c show that field monitoring, numerical simulation, and model testing are in good agreement in terms of the overall deformation pattern: the maximum surface settlement is concentrated near the tunnel axis, and settlement in the middle part

of the building is greater than that at the edges. All three methods also identify excavation of the upper bench of the right pilot tunnel beneath the building as the critical stage during which settlement develops rapidly. However, compared with the model-test and numerical results, the field curves exhibit stronger local fluctuations and a deeper local settlement trough, which is related to the methodological limitations summarized below.

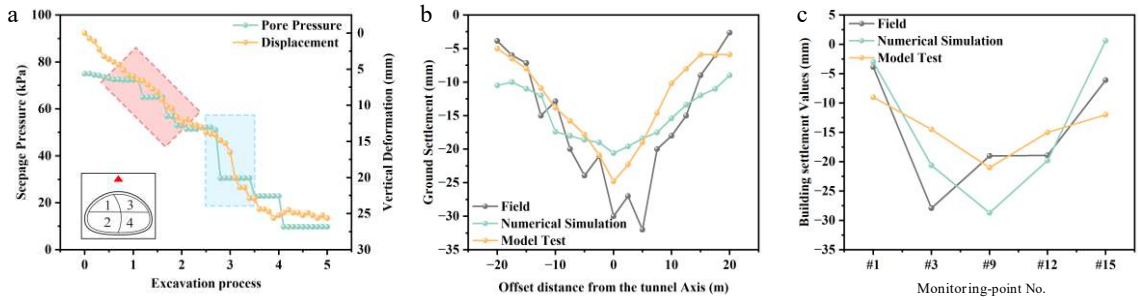

Figure 8. Comparison and validation of deformation responses. **a** Seepage pressure and vertical displacement at crown monitoring points; **b** surface settlement obtained from field monitoring, the model test and numerical simulation; and **c** settlement and monitoring-point layout for the overlying building section.

Based on the above findings, the stage in which the upper bench passes beneath the building should be regarded as the key risk-control window in engineering practice. Joint monitoring should therefore be strengthened for crown displacement, ground-surface settlement above the tunnel axis, shallow pore water pressure, and the foundations and critical first-floor joints of the building. In water-rich strata, particular attention should be paid to the correspondence between rapid pore-pressure dissipation and accelerated settlement. For buildings with significant offset or unfavorable crossing angles, differential settlement, tilting, torsion, and local internal-force concentration should also be specifically monitored.

This study still has certain methodological limitations. The physical model inevitably has limitations in reproducing the scale effect of seepage behaviour and the correspondence between drainage and deformation. The numerical model adopts idealized assumptions regarding stratum heterogeneity and building stiffness. Field monitoring data are also constrained by the layout of discrete monitoring points and the conditions for continuous observation. Overall, the tunnel-building feedback effect identified in this study should be understood as a multi-factor coupled process jointly governed by staged excavation, fluid-solid coupling response, and three-dimensional spatial relationship. The main significance of this work lies in clarifying how construction sequence, groundwater dissipation, and the spatial position of buildings jointly control the deformation sequence, response magnitude, and distribution pattern of shallow-buried, extra-large-span tunnels in coastal urban areas during undercrossing beneath buildings.

5. Conclusion

This study developed a coupled hydro-mechanical model test system and carried out a corresponding simulation test on the excavation of a shallow-buried, extra-large-span tunnel in coastal strata. The same process was further verified by numerical

simulation using the finite difference method, and the validity of the results was evaluated against field monitoring data. The main conclusions are as follows:

(1) For shallow-buried, extra-large-span tunnels undercrossing existing buildings, excavation of the upper bench of the right pilot tunnel beneath the building is the critical construction stage controlling surrounding-rock deformation, ground-surface settlement, and building response. At this stage, crown displacement, surface settlement, stress release, and pore-pressure dissipation are all most pronounced, indicating that construction staging plays a decisive role in the evolution of excavation-induced risk.

(2) Groundwater seepage significantly amplifies the response to excavation disturbance. During excavation, drainage paths gradually develop near the crown and arch shoulders, where rapid pore-pressure dissipation leads to effective-stress redistribution and further induces additional compression and settlement. The numerical results show that, when groundwater is considered, the maximum crown displacement increases by 27.3% compared with the case without seepage, indicating that tunnel deformation in water-rich strata should be regarded as a typical fluid-solid coupling problem.

(3) Building loading and its spatial relationship with the tunnel jointly govern the response patterns of both the strata and the structure. When the building is located directly above the tunnel, the ground-surface settlement trough remains approximately symmetric overall, but becomes deeper and narrower under the effect of building loading. When offset or unfavorable crossing angles exist between the building and the tunnel, the settlement trough evolves into an asymmetric distribution, and the building becomes more susceptible to differential settlement, tilting, torsion, and local stress concentration. Therefore, the spatial relationship controls not only the magnitude of settlement, but also the distribution pattern of unfavorable structural responses.

(4) The model test, numerical simulation, and field monitoring show good agreement in terms of the overall deformation pattern and identification of the critical construction stage, indicating that the interpretation of the tunnel-building interaction mechanism proposed in this study is of practical engineering credibility. For similar projects, the stage in which the upper bench passes beneath the building should be treated as the key risk-control window, and joint monitoring should be strengthened for crown displacement, ground-surface settlement above the tunnel axis, shallow pore water pressure, and the foundations and critical first-floor joints of the building.

(5) The conclusions of this study are mainly applicable to shallow-buried, extra-large-span tunnels in coastal water-rich strata that closely approach or undercross existing buildings. The main value of this work lies in revealing the coupled mechanism among construction sequence, groundwater dissipation, and the spatial relationship between tunnel and building. Owing to the limitations associated with a single engineering case, the scale effect of the physical model, and the idealized treatment adopted in the numerical model, the present study is more suitable for clarifying mechanisms and response trends. More systematic parametric investigations are still needed with respect to load level, foundation type, offset distance, crossing angle, and hydrogeological conditions.

Funding Declaration

Research in this paper is supported by the National Natural Science Foundation of China (Grant No. 42307228, 42293351 and U2468221), Beijing Natural Science Foundation (Grant No. 8252018), and Open Fund of State Key Laboratory of Geohazard Prevention and Geoenvironment Protection (Chengdu University of Technology) (Grant No. SKLGP2024K013).

Author Contributions

Hanming Zhang: Writing-Original draft preparation, Reviewing, Editing. Zhuangzhuang Guo: Writing-Original draft preparation, Reviewing, Editing. Fanmeng Kong: Conceptualization, Methodology, Reviewing, Editing. Yiguo Xue: Conceptualization, Methodology, Reviewing, Editing.

Data availability

The data underlying this article will be made available on reasonable request.

Competing interests statement

The authors declare that they have no known competing financial interests or personal relationships that could have appeared to influence the work reported in this paper.

References

[1] Bayati, M. & Hamidi, J. K. A case study on TBM tunnelling in fault zones and l essons learned from ground improvement. *Tunn. Undergr. Space Technol.* **63**, 162–1 70; https://doi.org/10.1016/j.tust.2016.12.006 (2017).

[2] Zhang, J., Wang, X. & Liu, T. Study on the influence of undercrossing tunnel on existing metro lines and surrounding environment. *J. Undergr. Space Eng.* **8**, 1088–1093 (in Chinese) (2012).

[3] Wang, J. et al. Numerical simulation of ultra-shallow buried large-span double-arch tunnel excavated under an expressway. *Appl. Sci.* **12**, 39; https://doi.org/10.3390/ap p12010039 (2022).

[4] Xu, J. et al. Effects of foundation pressure and building stiffness on tunnel–separat ed footing interaction. *Can. Geotech. J.* **62**, 1–20; https://doi.org/10.1139/cgj-2024-0 744 (2025).

[5] Dong, Z. et al. Grouting-induced ground heave and building damage in tunnel con struction: a case study of Shenzhen Metro. *Underground Space* **7**, 1175–1191; http s://doi.org/10.1016/j.undsp.2022.04.002 (2022).

[6] Zhang, L., Wang, Z., Zhang, W. & Liu, S. Sandy aquifer collapse mechanism and accident treatment of the Qingdao Metro tunnel. *Front. Earth Sci.* **11**, 1293258; htt ps://doi.org/10.3389/feart.2023.1293258 (2023).

[7] Li, Y. et al. Influence of tunnel excavation on the deformation of a frame buildin g. *Buildings* **13**, 810; https://doi.org/10.3390/buildings13030810 (2023).

[8] Zhang, X., Li, J., Chian, S. C. & Wang, Q. Monitoring of ground and building se ttlements induced by tunneling based on terrestrial LiDAR data: a case study in Si ngapore. *Smart Constr.* **1**, 0003; https://doi.org/10.55092/sc20250003 (2025).

[9] Dong, H. et al. A highly brittle similar material for rock burst simulation tests: qu antitative evaluation and experimental validation. *Rock Mech. Rock Eng.*; https://doi. org/10.1007/s00603-025-05056-9 Advance online publication. (2025).

[10] Zan, W. et al. Experimental and applied research on similar materials to granular mixtures for solid–liquid coupling model test of an underwater tunnel. *Constr. Buil*

781 *d. Mater.* **416**, 135170; https://doi.org/10.1016/j.conbuildmat.2024.135170 (2024).
782 [11] Zhao, D. et al. Similar model test of a mudstone-interbedded–sandstone-bedding r
783 ock tunnel. *Tunn. Undergr. Space Technol.* **140**, 105299; https://doi.org/10.1016/j.tus
784 t.2023.105299 (2023).
785 [12] Li, S. et al. Development and application of a new type of similar material for f
786 luid–solid coupling model tests in underground engineering. *Chin. J. Rock Mech. E*
787 *ng.* **31**, 1128–1137 (in Chinese) (2012).
788 [13] Jiang, B. et al. Development of physical model test system for fault-slip-induced
789 rockburst in underground coal mining. *J. Rock Mech. Geotech. Eng.* **17**, 2227–223
790 8; https://doi.org/10.1016/j.jrmge.2024.04.003 (2025).
791 [14] Liu, H. et al. A true triaxial dynamic multi-field coupling testing apparatus for u
792 nderstanding the failure behavior of deep hard rocks. *Measurement* **258B**, 119074;
793 https://doi.org/10.1016/j.measurement.2025.119074 (2026).
794 [15] Zhang, W. et al. Visualization and digitization of model tunnel deformation via tr
795 ansparent soil testing technique. *Underground Space* **7**, 564–576; https://doi.org/10.1
796 016/j.undsp.2020.05.004 (2022).
797 [16] Ritter, S., Giardina, G., DeJong, M. J. & Mair, R. J. Centrifuge modelling of bui
798 lding response to tunnel excavation. *Int. J. Phys. Model. Geotech.* **18**, 146–161; htt
799 ps://doi.org/10.1680/jphmg.16.00053 (2018).
800 [17] Xu, J., Franza, A., Marshall, A. M., Losacco, N. & Boldini, D. Tunnel–framed b
801 uilding interaction: comparison between raft and separate footing foundations. *Géote*
802 *chnique* **71**, 631–644; https://doi.org/10.1680/jgeot.19.P.393 (2021).
803 [18] Liu, T. et al. Deformation patterns and control of existing tunnels induced by coa
804 stal foundation pit excavation. *J. Mar. Sci. Eng.* **13**, 773; https://doi.org/10.3390/jms
805 e13040773 (2025).
806 [19] Ai, X., Yu, J. & Xu, L. Analysis of the effect of tunnel construction on frame s
807 tructure buildings in Xiamen Airport Road. *Proc. 11th Int. Symp. Struct. Eng.* **I–II**,
808 940–946; https://doi.org/10.1109/MACE.2011.5987351 (2010).
809 [20] Ding, Z. et al. Numerical investigation of 3D deformations of existing buildings i
810 nduced by tunnelling. *Geotech. Geol. Eng.* **37**, 2611–2623; https://doi.org/10.1007/s1
811 0706-018-00781-1 (2019).
812 [21] Namazi, E., Mohamad, H. & Hajihassani, M. 3D behaviour of buildings due to t
813 unnel-induced ground movement. *Transp. Geotech.* **31**, 100661; https://doi.org/10.10
814 16/j.trgeo.2021.100661 (2021).
815 [22] Balkaya, M. The effects of tunnel horizontal distance on the vertical deformations
816 of an adjacent building. *AIP Conf. Proc.* **1702**, 170014; https://doi.org/10.1063/1.4
817 938949 (2015).
818 [23] Namazi, E., Mohamad, H., Hong, A. K. B. & Yassin, A. Y. M. Twist deformatio
819 n of buildings from ground movements due to skewed-tunnel excavation. *in Geotec*
820 *hnical Aspects of Underground Construction in Soft Ground* (eds Yoo, C., Park, S.-
821 W., Kim, B. & Ban, H.) 281–286 (CRC Press, 2014).
822 [24] Wei, G., Chen, D. & Hong, J. Effect analysis of double-O-tube shield tunnel cro
823 ssing frame structure building with 30°. *Disaster Adv.* **5**, 447–451 (2012).
824 [25] Yu, L. et al. Analytical prediction of strip foundation building response to shallo

w tunneling considering the tunneling process. *Appl. Sci.* **12**, 4656; https://doi.org/10.3390/app12094656 (2022).

[26] Duan, S. et al. The collapse mechanism in a subsea tunnel passing through the fault: a model test study. *Environ. Earth Sci.* **83**, 513; https://doi.org/10.1007/s12665-024-11792-y (2024).

[27] Gong, H. et al. Large deformation characteristics and mechanism analysis of excavating shallow-buried tunnel in reclamation areas. *Bull. Eng. Geol. Environ.* **84**, 26; https://doi.org/10.1007/s10064-024-04067-0 (2025).

[28] Wang, C. et al. Three-dimensional hydro-mechanical coupling numerical simulation of shield-driven cross-river twin tunnels: a case study. *Underground Space* **16**, 106–125; https://doi.org/10.1016/j.undsp.2023.09.010 (2024).

[29] Zhao, C., Zhang, Z. & Lei, Q. Role of hydro-mechanical coupling in excavation-induced damage propagation, fracture deformation and microseismicity evolution in naturally fractured rocks. *Eng. Geol.* **289**, 106169; https://doi.org/10.1016/j.enggeo.2021.106169 (2021).

[30] Zhang, D.-M., Chen, C.-C. & Zhang, D.-M. Ground surface movement of shallow-buried large-sectional tunnel under full-ring pipe-jacking roof and ground freezing. *Tunn. Undergr. Space Technol.* **127**, 104600; https://doi.org/10.1016/j.tust.2022.104600 (2022).

Supplementary Files

This is a list of supplementary files associated with this preprint. Click to download.

- SupplementaryFigures.docx